MATERIALS SCIENCE

Alignment and actuation of liquid crystals via 3D confinement and two-photon laser printing

Li-Yun Hsu[1]†, Santiago Gomez Melo[2,3]†, Clara Vazquez-Martel[1], Christoph A. Spiegel[1], Falko Ziebert[2,3], Ulrich S. Schwarz[2,3]*, Eva Blasco[1]*

Liquid crystalline (LC) materials are especially suited for the preparation of active three-dimensional (3D) and 4D microstructures using two-photon laser printing. To achieve the desired actuation, the alignment of the LCs has to be controlled during the printing process. In most cases studied before, the alignment relied on surface modifications and complex alignment patterns and concomitant actuation were not possible. Here, we introduce a strategy for spatially aligning LC domains in three-dimensional space by using 3D-printed polydimethylsiloxane-based microscaffolds as confinement barriers, which induce the desired director field. The director field resulting from the boundary conditions is calculated with Landau de Gennes theory and validated by comparing experimentally measured and theoretically predicted birefringence patterns. We demonstrate our procedures for structures of varying complexity and then employed them to fabricate 4D microstructures that show the desired actuation. Overall, we obtain excellent agreement between theory and experiment. This opens the door for rational design of functional materials for 4D (micro)printing in the future.

INTRODUCTION

The design and precise fabrication of smart materials are quickly growing fields with many applications ranging from microfluidics and microsensors to biomedicine (*1*). For example, microswimmers and microwalkers that mimic biological microorganisms have been used to achieve autonomous operations, including cargo transportation, molecular sensing, and drug delivery in response to changes in their biological environment (*2*–*5*). Two-photon laser printing (2PLP), an additive manufacturing technique based on two-photon polymerization, has had a profound impact on fabricating these smart microsystems due to its ability to construct three-dimensional (3D) structures with submicrometer resolution. The use of printable smart materials is key to combine the geometry of a printed structure with specific stimuli-responsive features and functionalities (*6*, *7*). Among these smart materials, liquid crystal elastomers (LCEs) are unique due to their ability to perform strong mechanical actuation in response to an external stimulus, usually temperature (*8*–*11*). This response relies on their large and reversible volume change upon reorientation of pre-aligned liquid crystal (LC) molecules (mesogens) at the nematic-to-isotropic transition.

In recent years, remarkable efforts have been dedicated to advancing the fabrication of LCE microsystems using 2PLP, especially by designing new (multi)responsive printable systems (*12*–*17*). While these developments represent major advances in the field, it is important to note that many of the previously reported examples are restricted to one-directional movements, which limits their ability to enhance the complexity of actuation patterns. In the previously reported literature, a tedious stepwise or modular fabrication process was necessary to achieve bidirectional actuation (*18*, *19*). This problem results from the challenges associated with controlling the orientation of LCs in 3D, which then determines the actuation behavior of LCEs (*20*). To control the alignment of the LC monomers during 3D printing, the most straightforward approach is the use of functionalized surfaces. This involves the use of an alignment cell, where the LC ink is filled into the gap between two surface-modified glass slides. The modified surfaces, including polymer coating or surface rubbing, enforce a universal director field in the whole LC material, and thus resulting in only one simple actuating pattern. The limitations on programing LC orientation within an alignment cell are two-folds: (i) The surfaces from the top and the bottom glass have a direct influence on orienting LC molecules only when they are in contact with the surfaces, while the ones at the core layers can only be aligned indirectly, by molecular interactions propagated from the anchored molecules. Therefore, surface alignment methods are generally restricted to a cell thickness of 100 μm. (ii) To locally control alignment, very complex methods such as lithography patterning (*21*, *22*) or microrubbing technique (*23*) are required to achieve the desired spatial accuracy. For example, 2PLP has also been used for the fabrication of micro surface-relief gratings, which offers anchoring energy to LCs enabling 2D and 2.5D surface alignment (*21*, *22*, *24*, *25*). Recently, Smalyukh and coworkers (*26*, *27*) have reported a novel alignment approach using nematic colloids (e.g., microprinted knotted and interlinked particle geometries) that further advance the possibilities of aligning LC media in 3D. Furthermore, the group studied the effect of chiral LC colloids (*28*). However, in these approaches, the alignment pattern itself is usually uniform and there have been only a few reported approaches aiming at allowing flexible alignment manipulation of printable LC (LC inks) to control the alignment and therefore, actuation in the final 3D-printed microstructure in a spatially modulated fashion. For instance, in a previous work, we demonstrated the capability to alter the alignment of LC ink in situ by applying electric fields during the printing process (*29*, *30*). This approach enabled the fabrication of LCE microstructures with intricate alignment designs, showcasing complex actuation. However, this method requires very special technical expertise to realize the necessary customized setup.

In this study, we present a method for straightforward control of LC alignment in 3D by using polydimethylsiloxane (PDMS)

[1]Institute for Molecular Systems Engineering and Advanced Materials (IMSEAM), Heidelberg University, Im Neuenheimer Feld 225, Heidelberg 69120, Germany. [2]Institute for Theoretical Physics, Heidelberg University, Philosophenweg 19, Heidelberg 69120 Germany. [3]BioQuant, Heidelberg University, Im Neuenheimer Feld 267, Heidelberg 69120 Germany.
*Corresponding author. Email: schwarz@thphys.uni-heidelberg.de (U.S.S.); eva.blasco@uni-heidelberg.de (E.B.)
†These authors contributed equally to this work.

microscaffolds using a commercially available two-photon 3D laser printing setup. It has been reported that the hydrophobic properties of PDMS surfaces induce a perpendicular anchoring effect of LC molecules (*31*, *32*). However, the fabrication of PDMS scaffolds has been limited to conventional molding method, using a PDMS-based master mold or microfluidics to manipulate LC orientations (*33*, *34*), where the geometries and resolutions were very limited. Leveraging the capabilities of 2PLP, PDMS-based microscaffolds can now be 3D printed with higher resolution and arbitrary shapes, such as microchannels, microwells, and other complex geometries. Here, we demonstrate that these 3D-printed PDMS-scaffolds can be used to control the nematic orientation in 3D. To prove the success of our method, we calculated the expected orientation field with Landau de Gennes theory for the given boundary conditions and then compared the measured and simulated birefringence of the different samples. The excellent agreement between experiment and theoretical calculation has proven that the level of controlling LC directors is not only limited to the top and bottom surfaces but also extends along the z axis. Furthermore, the method was also applied to investigate the actuation of 3D-printed LC microstructures with temperature and we observed exactly the deformations predicted with an elastic theory. This opens the door for 4D (micro)printing of smart materials with preprogrammed actuation behavior. In Fig. 1, we show a schematic overview of our workflow.

RESULTS

Fabrication of PDMS-based 3D microscaffolds and LC alignment

As a first step, PDMS 3D microscaffolds were fabricated via 2PLP (see fig. S1), which offers several advantages compared to the conventional microreplica molding methods. 2PLP enables not only the construction of multiple 3D scaffolds with varied geometries in a single print but also avoids rough surfaces and artifacts that are typically observed when using molding methods, causing undesirable topological defects (*31*, *35*, *36*). For this purpose, a commercially available PDMS-based ink (IP-PDMS, Nanoscribe GmbH) was used (*37*). Because of the soft elastomeric properties of PDMS, a specific printing protocol was developed involving first printing a densely cross-linked contour at a slower scanning speed (20 mm/s, 30 mW) and then rapidly filling the interior (100 mm/s, 40 mW) to ensure good structural stability.

Once optimized the parameters for the fabrication of the 3D microscaffolds, the PDMS-induced alignment effect was examined by fabricating an alignment cell as depicted in Fig. 1. Specifically, the glass substrate with the printed PDMS scaffolds and a second substrate were glued together using spacers in between to define the cell thickness. Subsequently, a liquid crystalline material, i.e., E7 mixture, was infiltrated (see details in Materials and Methods). To prove the effect of the PDMS scaffolds, the glass substrates used in the study were spin-coated with polyimide (SE-5661, Nissan Chemicals). This coating ensured that LC molecules are pristinely homeotropically aligned. As a result, when observed under a polarized optical microscope (POM), a dark, nonbirefringent background is observed, regardless of the orientation of the sample. However, if the aligning vector is affected by the PDMS and no longer perpendicular to the substrate, this disturbance should be identified by the resulting pattern under the POM. The relationship between PDMS geometry and the induced alignment effect was carefully investigated by designing two types of PDMS microscaffolds, as discussed below.

Planar alignment

The first type of scaffolds consisted of microchannels formed by two parallel PDMS blocks, designed to reorient the LC director field in an orthogonal fashion to the PDMS surfaces, thereby inducing a

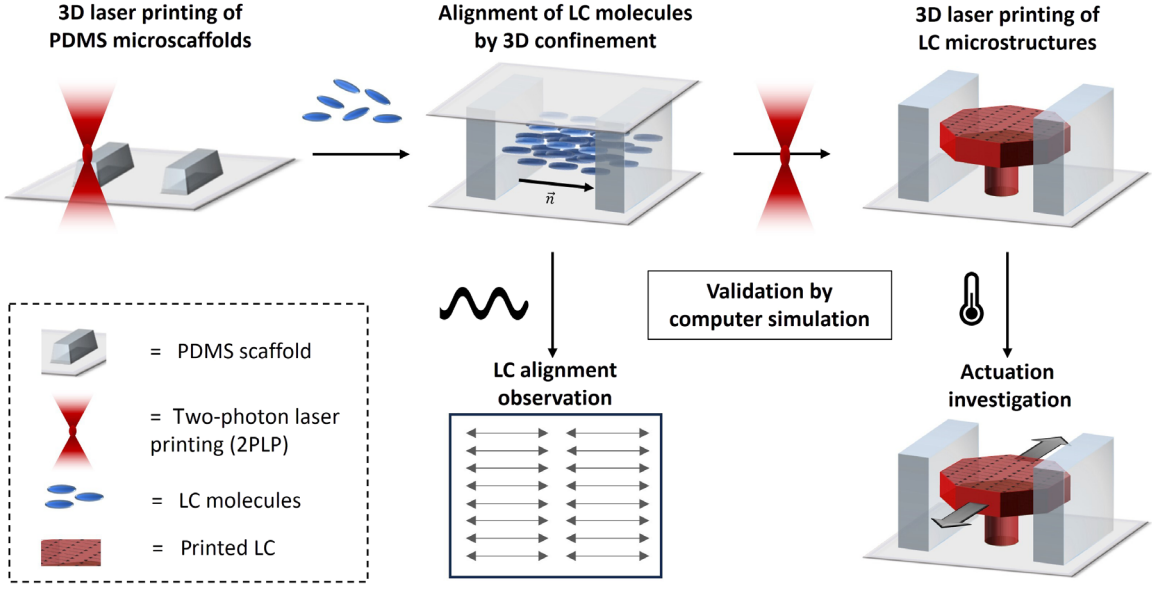

Fig. 1. Schematic illustration of the workflow. The alignment of LC molecules (blue ovals) can be manipulated with the geometry of the PDMS microscaffolds (gray). The aligned LC molecules can be used for the subsequent fabrication of 3D LCE microstructures (red) using 2PLP. The induced alignment fields (black patterns) are preserved within the LCE microstructures. The director field resulting from the boundary conditions is calculated with Landau de Gennes theory and validated by comparing experimentally measured and theoretically predicted birefringence patterns. The actuation of the 4D-printed microstructures with temperature is predicted by an elastic theory and validated by comparison with the actuated shape.

planar alignment between two partitions (Fig. 2A). The microchannels were fabricated with a constant thickness of 20 μm and a length of 100 μm (Fig. 2B). To determine the effect of the PDMS geometry on the LC alignment, the height (*H*) or the channel width (*W*) of these channels was systematically varied (Fig. 2C). The effect was assessed by examining the optical density (OD) obtained from POM images taken at the centerline of the microchannels and comparing to theoretical predictions based on Landau de Gennes theory combined with Jones calculus for optical intensity calculations (see section S2 for details) (*27*–*28*, *38*–*40*). The simulated director fields in Fig. 2C demonstrate that narrower channels result in a predominantly planar alignment parallel to the plane of the substrate. As the channel was widened, alignment perpendicular to the substrate became energetically favorable at the center, resulting in the central near-zero intensity region observed in both POM and the simulated optical experiment. To further quantify these orientation effects depending on the geometry, we plotted the mean OD as a function of the aspect ratio $\eta = H/W$ (*31*) of the PDMS channel (Fig. 2D). When the width *W* was held constant at 30 μm (left), the presence of a polydomain (partially induced planar alignment and the pristine homeotropic alignment) was observed within the channel when the height *H* was below 20 μm. This was indicated by a high OD value, resulting from a dark background in the images. Contrarily, when the aspect ratio $\eta = H/W$ exceeded 0.67, substantially lower OD values were observed, which were attributed to the bright birefringence signal falling within the range of 0.7 to 0.85. This revealed the disruption of the pristine homeotropic alignment over a large distance. A similar effect was also observed in the corresponding experiment where we expanded the width (*W*) while maintaining a constant height (*H*) of 30 μm (right). The mean OD remained in the range of

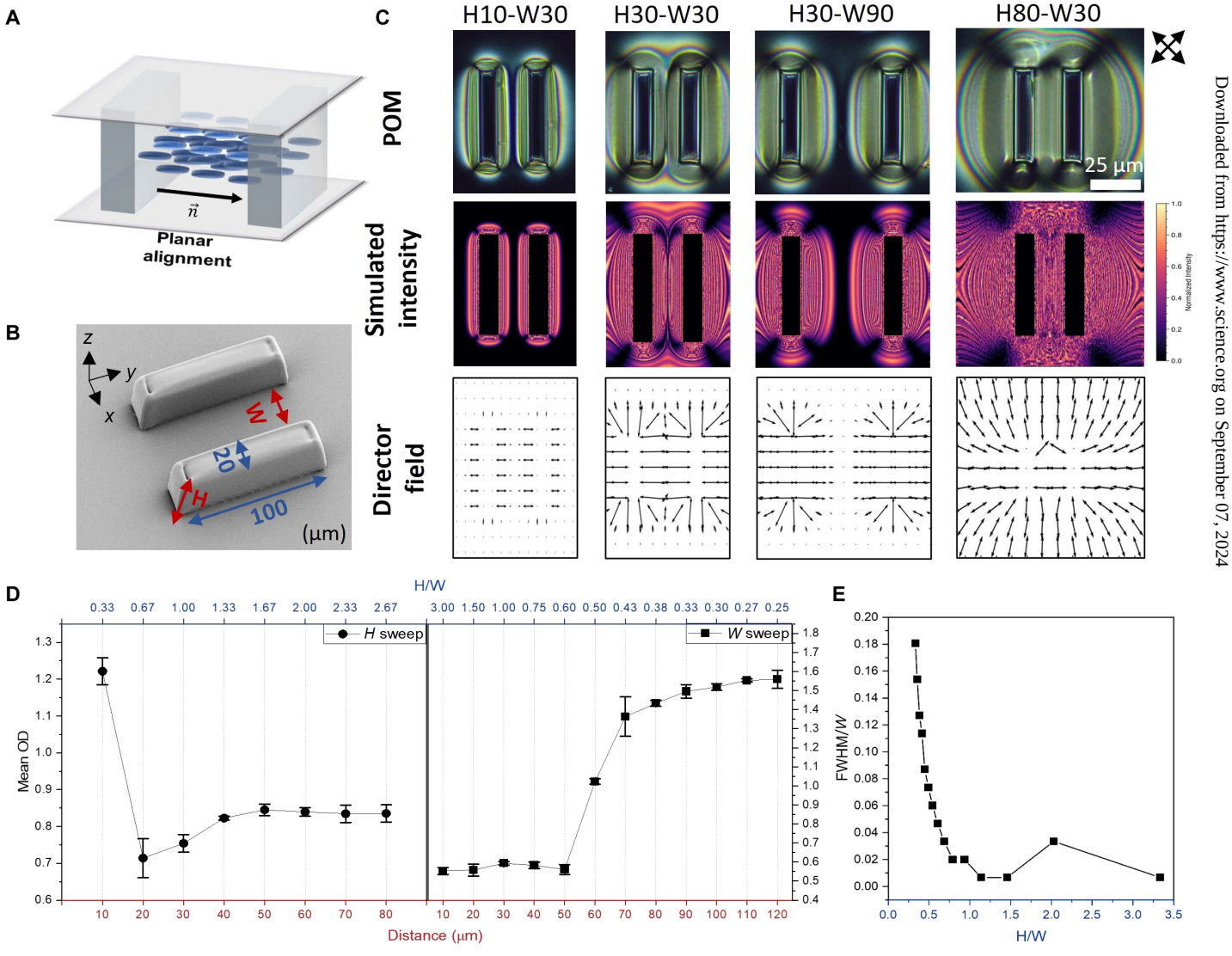

Fig. 2. Planar alignment using PDMS microscaffolds. (**A**) Schematic illustration of LC molecules orientation within a PDMS microchannel. (**B**) Electron microscopy image of the PDMS blocks. (**C**) LC alignment with E7 mixture induced by PDMS microchannels with varied height (*H*) and width (*W*) measured by POM (top, orientation of the polarizers is indicated by the arrows). Simulated intensity map (center) and director field at the top of the scaffold (bottom) of alignment effect induced by PDMS microchannels. (**D**) Mean optical density (OD) acquired from POM images, with varied channel height (left) or width (right), plotted against their aspect ratio *H*/*W* ($n = 5$). (**E**) FWHM of simulated intensity normalized by *W* and plotted as a function of aspect ratio *H*/*W*.

0.5 to 0.6 when W was below 50 μm but increased two to threefold once the width exceeded this threshold. The findings from this second experiment further verified that a PDMS channel with $\eta > 0.60$ was expected to induce planar monodomains. The same conclusions were reached from the computer simulations by plotting the full width at (intensity) half maximum (FWHM) as a function of the aspect ratio (Fig. 2E). For $\eta < 0.75$ the FWHM/W increased sharply, indicating the existence of a region with pristine alignment and no intensity. Above this threshold, the FHWM/W dropped asymptotically to 0, implying planar alignment. We believe that this threshold matches the experimentally obtained critical value of $\eta = 0.60$. The remaining differences mainly result from uncertainties in the thermotropic and elastic parameters of the Landau de Gennes potential, as well as from the frequency dependence of the ordinary and extraordinary refractive indices.

Radial alignment

To induce LC radial alignment, PDMS 3D microscaffolds consisting of a cylindrical cavity were fabricated (Fig. 3A). Following the same procedure as before, LC cells were prepared and the E7 mixture was subsequently infiltrated to investigate the effect of geometry in the alignment (Fig. 3B). It should be noted that in the design of these 3D microscaffolds, "microtrench" features were implemented. The introduction of these features in the geometry design is twofold: (i) to effectively reduce the interfacial tension between the PDMS bulk and the substrate and to prevent detachment during the solvent-washing process and (ii) to facilitate the successful infiltration of LC into the confined cavities, as shown as the cross patterns along the x and y axes in the POM images (Fig. 3C). The concentric LC topography observed by POM inside the microscaffolds suggested the formation of a radial domain, further confirmed by the simulated director field. Analogous to the planar case, primarily radial alignment is observed for narrower cylindrical wells, whereas larger cylinders result in the coexistence of radial alignment near the walls and z alignment at the center. The latter results in high optical extinction at the center, observed in POM and confirmed by the simulated optical experiment. Consequently, the intensity profiles again provide a measure for the length scale at which the director rotates from the radial configuration to the z alignment.

We next studied the onset of z alignment at the center and its effective range as a function of the aspect ratio ($\eta = R/H'$), defined in this case by the radius (R) and the height (H') of the cylindrical cavity (Fig. 3B). When the cavities remained at a constant height of 30 μm, the difference of the OD value between the circular center and the LC-PDMS interface (ΔOD) notably increases as the radius exceeded 37.5 μm, indicating the formation of a polydomain (see section S3 for details). In the POM images, we observed the formation of black circular areas, whose size expanded with increasing cavity radius. This may be due to the competition between the intermolecular interactions of the re-anchored LC molecules and those initially aligned to the functionalized substrate. In other words, the surface ratio between the cylindrical well and the substrate surface determines the resulting director field within the PDMS microscaffold. As shown by simulations, when the FWHM/R starts increasing above $\eta' = 0.5$ to 0.6, the presence of a z-aligned domain becomes more prominent than the predominant radial alignment (Fig. 3D and fig. S2). In general, a similar director field pattern is obtained for different scaffold sizes as long as their aspect ratio remains constant, because all material length scales are much smaller than the printed structures. In fig. S3, we theoretically compared two cylindrical wells with different sizes, but with the same aspect ratio of $R/H = 1.65$. This yielded indistinguishable director fields and nearly identical birefringence patterns.

Furthermore, we exploited the freedom of 2PLP for the creation of complex 3D microscaffolds and tested the radial alignment using not only cylindrical microcavities but also other geometries. To this aim, we designed a 3D model in which the microcavities to accommodate the LC material can be precisely positioned in 3D. In particular, three different types of confining shapes, cylindrical, triangular, and floral, were integrated within a 3D block ($90 \times 90 \times 90$ μm^3) at different heights (30 μm space between them) (Fig. 3E). As before, the incorporated "microtrenches" enabled the infiltration of the LC molecules in each microcavity. The formation of distinct radial patterns for the three shapes was clearly visible by POM.

Printing LCE microstructures with tailored alignment profile in 3D

As a next step, the concept of using PDMS microscaffolds to tailor LC alignment in 3D was extended to the fabrication of microstructures using 2PLP. It is expected that the alignment patterns achieved due to the presence of PDMS microscaffolds are translated into the printed 3D microstructure and therefore, new complex actuations can be accomplished that are unattainable using conventional methods such as surface alignment. Thus, for this purpose, we printed LCE 3D microstructures in the vicinity of the preprinted PDMS microscaffolds (Fig. 4A) and investigated the influence in the alignment and to prove that this alignment is retained after the fabrication process.

To generate microstructures, the LC E7 mixture used in the previous section was replaced with a printable LC ink that can be photopolymerized via 2PLP. This ink was adapted from our previous work (*13*, *30*) and consisted of a mixture of LC monomer [4-(6-acryloyloxyhexyloxy) phenyl ester (C6BP), 29.4 wt %], cross-linkers {1,4-bis[4-(3-acryloyloxypropyloxy) benzoyloxy]-2-methylbenzene (RM257) and 4-[6-(acryloyloxy)hexyloxy]phenyl 4-[6-(acryloyloxy)hexyloxy] benzoate (C6BAPE), 14.7 wt % each}, a photoinitiator [phenylbis(2,4,6-trimethylbenzoyl)phosphine oxide (BAPO), 1.5 wt %], and an inhibitor [3,5-di-tert-4-butylhydroxytoluene (BHT), 0.5 wt %] to prevent thermal polymerization during the alignment process (see section S4). In addition, 39.2 wt % of E7 was included in the formulation to achieve optimal viscosity.

To demonstrate the possibility of manipulating the alignment in the microstructures, an octagonal plate (50×50 μm^2, side length 10 μm) was printed in different environments, starting with no PDMS microscaffold in the vicinity and then increasing the level of confinement by including more PDMS partitions until an octagonal cavity was formed (Fig. 4B). As shown in the POM images, the birefringence underwent progressive changes, as a result of the different alignments. Initially, the 3D-printed microstructure appeared mainly black due to pristine homeotropic alignment. With the placement of two parallel PDMS, it turned into a linear texture with a rotated orientation. Subsequently, it evolved into an octagonal pattern radiating from the center. Moreover, complex radial patterns, including cylindrical, triangular, and flower-like shapes, were introduced into printed LCE microstructures by adjusting the plate geometries to match the PDMS cavities (Fig. 4C). We could prove that the unique aspect of this approach, the capability to achieve a higher level of complexity and sophistication in the alignment patterning, can also be translated to the 3D-printed microstructures.

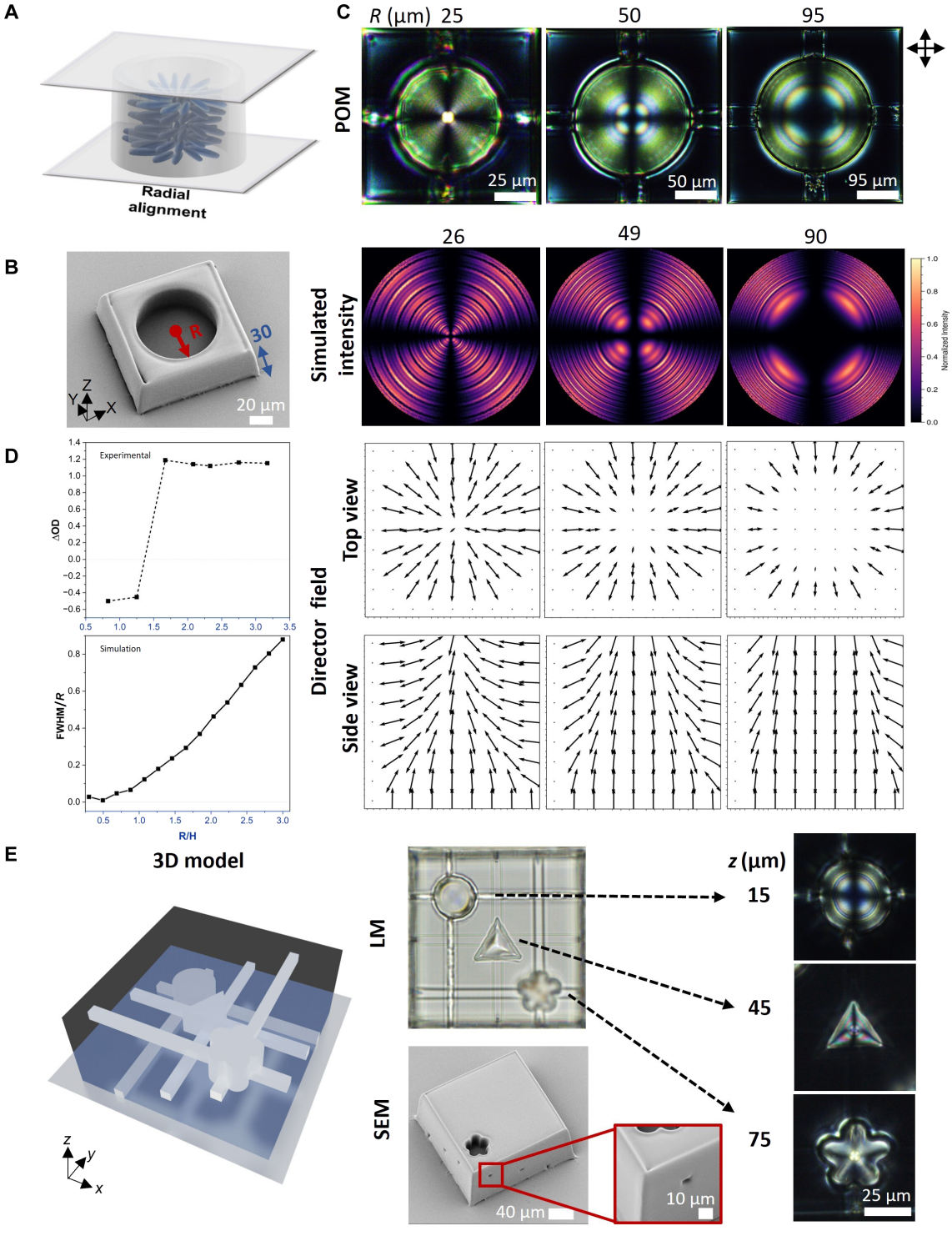

Fig. 3. Radial alignment using PDMS microscaffolds. (**A**) Schematic illustration of LC molecules orientation within PDMS cylindrical cavity. (**B**) Electron microscopy image of the cylindrical geometry with the trench design. (**C**) POM images (orientation of the polarizers is indicated by the arrows) of E7 mixture aligned within the cylindrical cavities with varied radius and their simulated intensity and director field at the top of the scaffold as well as in side view. (**D**) ΔOD (top), and FWHM/*R* (bottom) of the intensity maps at the circular center as a function of aspect ratio R/H. (**E**) 3D model, light microscopic (LM) and SEM images of a PDMS block integrated with three microcavities, in circular, triangular and flower shapes, at varied *z* coordinates. POM images of the E7 infiltrated block were taken with different focus depth.

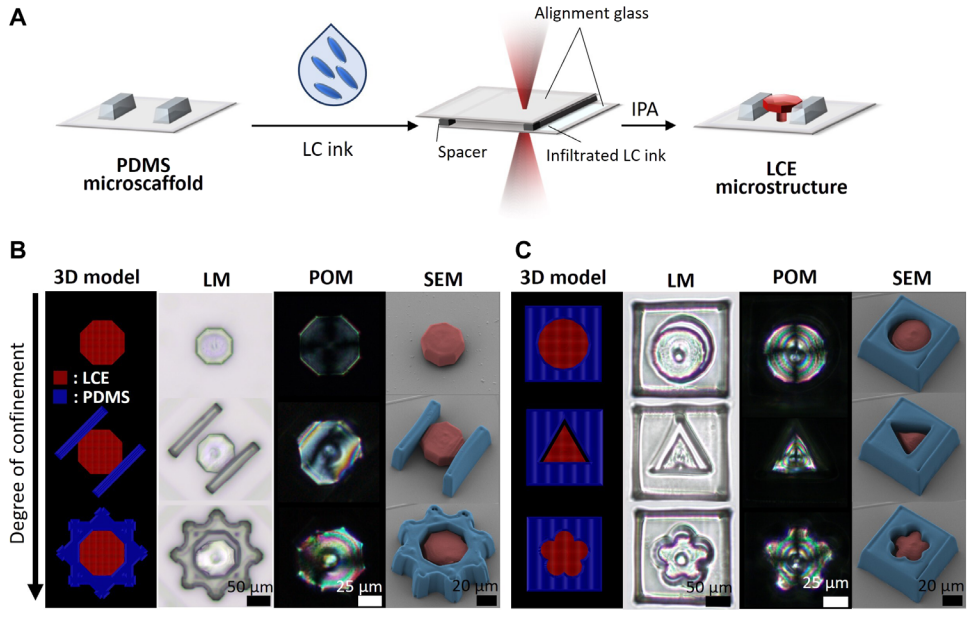

Fig. 4. 3D printing LCE microstructures with tailored alignment. (**A**) Schematic illustration of fabricating LCE microstructure (red) within a PDMS microscaffold. 3D model (top-down view), light microscope images (LM), POM images and SEM images (tilted view) of LCE structures (red) printed in PDMS microscaffolds (blue) with (**B**) different degree of confinement or (**C**) cylindrical, triangular and floral geometries. The plate of the LCE structure was positioned 15 μm above the substrate, corresponding to half the height of the PDMS microscaffolds ($H = 30$ μm). SEM images were false colored for clarity.

In addition to the LC topology induced by the PDMS scaffolds in the *xy* plane, we also explored the possibility of controlling the director field along the *z* axis. To this aim, a rectangular LCE microstructure ($37.5 \times 60 \times 15$ μm^3) was printed between PDMS partitions (Fig. 5, A to E). In addition to vertical scaffolds, which are orthogonal to the substrate as shown previously, other orientations and geometries of the PDMS microstructures were tested. These included PDMS scaffolds with a tilt of 45°, convex curves, and concave curves. To visualize the effect in the *z* direction, the POM images of the LCE microstructure were captured in side view. Compared to the reference structure printed without PDMS confinement (Fig. 5A), distinct printing outcomes and birefringence were observed for each structure. The microstructure printed in between the vertical scaffold (Fig. 5B) exhibited minimal birefringence, like the reference sample, as both the induced planar director and the pristine homeotropic alignment were oriented in line with the crossed polarizers. However, an additional layer (~16 μm) was observed on top of the reference sample, resulting in a greater overall height than the programmed model. This occurred due to the splitting of the laser focus while printing within a homeotropically aligned birefringent medium (*29*, *30*), as the focus splitting is less pronounced for planar director orientation. Also, the orientation of the LC director not only affected the laser focus differently but also resulted in distinct shrinkage behavior. As seen in Fig. 5C, the LCE microstructure exhibited a slight tilt due to the director being at 45° and radial LC topologies were observed in the LCE microstructures according to the curvature of the scaffolds (Fig. 5, C and D). For simulating the director field along the *z* direction, the same boundary conditions were used for the PDMS scaffold and the polyimide coated substrate. As seen in the last line of Fig. 5, the predicted director fields obey the prescribed boundary conditions. However, the simulated birefringence patterns do not always agree with the experimental observations. While the experiment and the simulation showed similar intensity profiles for the pristine sample (Fig. 5A) and the one within the concave scaffold (Fig. 5D), different profiles were found for the other cases. For example, because of the boundary effect from three surfaces (two walls and the substrate), nonzero intensity profiles were theoretically predicted between two straight walls (Fig. 5B) and for the tilted scaffold (Fig. 5C) under 45° polarization. However, experimentally, very low polarized signal was observed for these two cases. Also, a central intensity maximum at the central line between two straight walls (Fig. 5B) or at the field center of the convex scaffold (Fig. 5E) was predicted by the simulations but not in the experiment. Such disagreements might be attributed to different LC anchoring properties between the PDMS and polyimide surfaces (*32*, *41*, *42*), as the PDMS scaffolds appeared to more strongly influence the LC director than the polyimide surface. Furthermore, these differences could be caused by the nematic field distortion after the 3D printing process, e.g., because of the shrinkage and other deformations of the 3D structures during the processing. Overall, several cases show good agreement (especially A and D), while the agreement is worst for the most complex one (C).

Demonstrating 4D complex microactuation using PDMS-induced alignment

Last, we exploited the capabilities of the established methodology with PDMS microscaffolds to design LCE-based microactuators and to study, both experimentally and theoretically, their temperature response. As previously mentioned, actuation relies on the LC's nematic to isotropic transition. During this transition, the printed material will contract along the director. Thus, we aimed at inducing different alignments patterns to be able to program complex actuation patterns that are not attainable with conventional surface alignment.

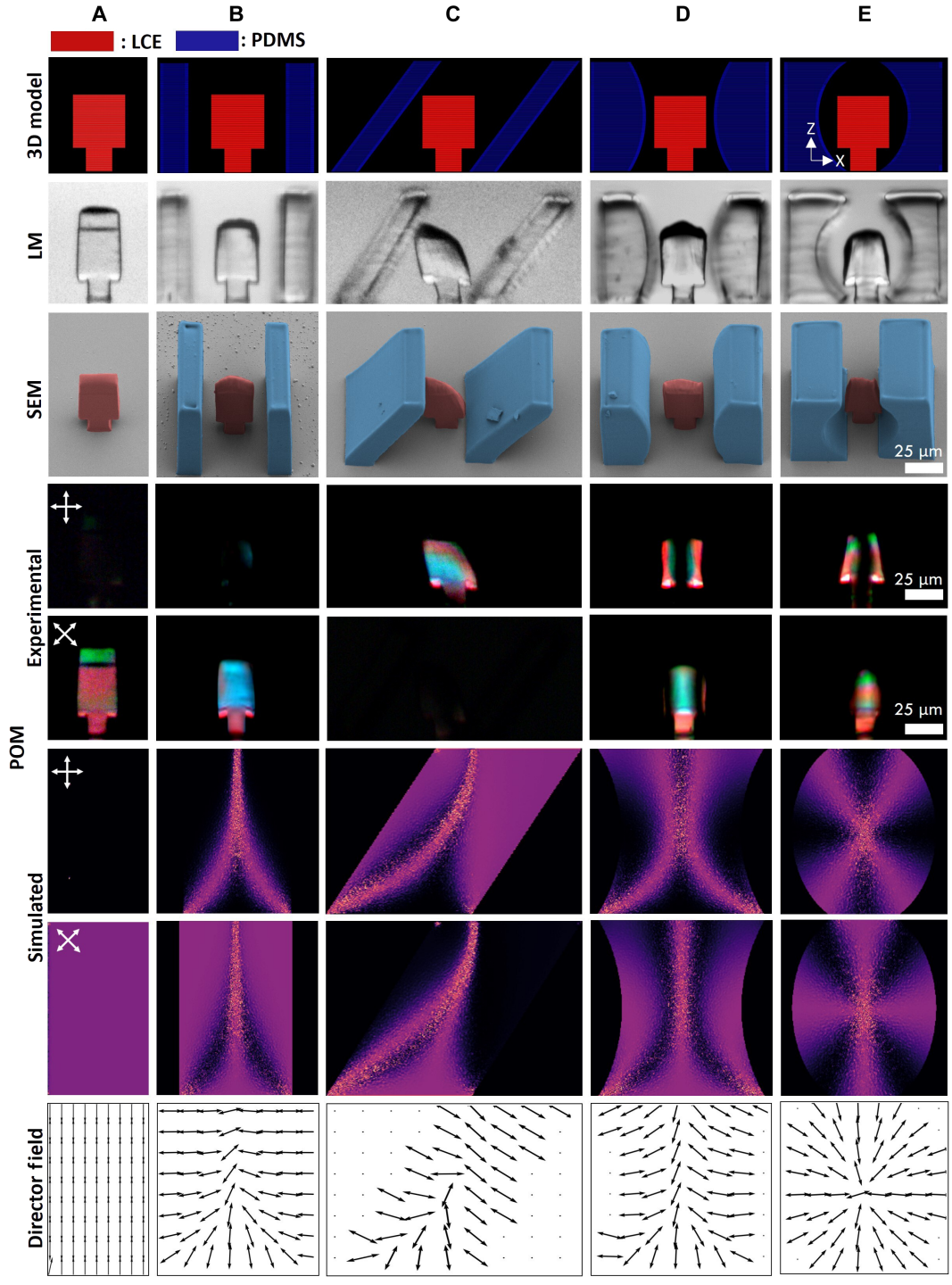

Fig. 5. Controlling the LC alignment along the *z* axis. Model, LM, POM (orientation of the polarizers is indicated by the arrows), and SEM images of LCE microstructure (red) printed within PDMS scaffolds (blue) with varied geometry (view from *y* axis) (**A** to **E**), as well as the director field and intensity profile obtained from simulations. SEM images were false-colored for clarity.

As a first step in the investigation of the microactuation, we printed LCE pillar arrays within three types of channel-like PDMS scaffolds in different orientations (Fig. 6, A and B). These pillar arrays consisted of a base plate and 5 × 5 pillars with a diameter of 4 μm. Their actuation was analyzed in an optical microscope with a heating stage. This allowed us to record the variations in the width and length of the array at room temperature and beyond the transition temperature. The impact of the PDMS channels on the LCE pillars became evident shortly after the removal of the unpolymerized ink. The pillars without PDMS channels in the vicinity, denoted as "pristine," underwent uniform shrinkage in both the *x* and *y* axes, primarily due to the homeotropic alignment enforced by the alignment surfaces on

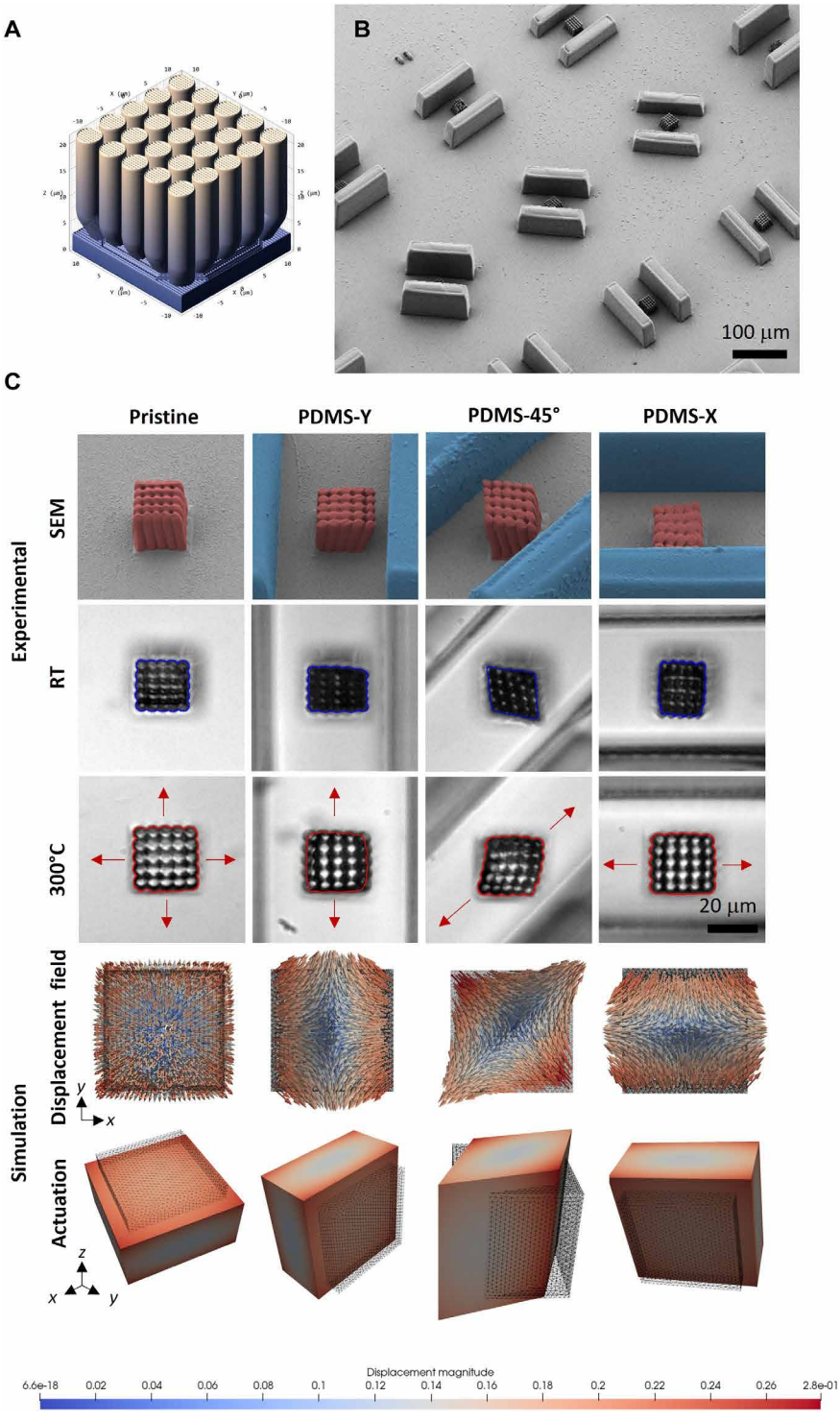

Fig. 6. 4D microactuation. (**A**) 3D model of a pillar array with dimension 20 × 20 × 20 μm^3 (radius, 2 μm). (**B**) SEM image of the pillar arrays within PDMS scaffolds with different orientations. (**C**) Temperature response of the pillar array, including SEM, optical images, and simulated mechanical actuation. The red arrows indicate the expanding direction of the arrays, corresponding to the difference between the simulated initial state (translucent) and the simulated activated state (saturated). The resulting displacement field was based on a simplified hyperelastic geometry for a uniform director field with orientation perpendicular to the PDMS scaffold. Units are rescaled so that the length of the undeformed cube is 1.

the glass cell. In contrast, the pillars printed within the channel-like scaffolds (labeled as "PDMS-Y," "PDMS-X," or "PDMS-45°," indicating the direction of the channels), exhibited a noticeable shrinkage along the expected alignment direction. For the channels rotated 45° (referred to as PDMS-45°), the pillar array formed a diamond shape, with the shorter diagonal aligned parallel to the channel (Fig. 6C). Once the temperature was increased above the transition temperature, an interesting observation emerged: While the pristine array expanded equally in both directions, in the three arrays printed inside the PDMS channels, the expansion was more pronounced in the direction parallel to the channel's orientation.

The mechanical actuation of the microactuators with the different director fields (Fig. 6C) was simulated using nonlinear morphoelasticity theory (see section S2) (*43*). In good agreement with the experiment, the theoretical model predicts the most prominent aspects of the deformation: As the structure is driven to the isotropic state, it contracts in the direction of the nematic director, and it expands in the perpendicular plane in order to meet the constraint of volume conservation. In the case of pristine alignment, the perpendicular plane to the director is parallel to the substrate, so the structure expands in both directions of this plane. In contrast, the perpendicular plane to the director in the presence of PDMS scaffolding is parallel to the scaffold, so the structure accordingly expands along the plane of the channel and contracts in the orthogonal direction. Thus, the simulations allow for a precise interpretation of the experimental deformation; it is a direct consequence of the interplay between the contraction along the programmed molecular orientation caused by the phase transition and the incompressibility requirement.

As the next step, we designed a more complex microactuator consisting of a free-rotating gripper ($40 \times 40 \times 30\ \mu m^3$) (Fig. 7). As expected, while symmetric actuation was observed for the pristine sample, under influence of the PDMS, the actuating behavior of the gripper within PDMS-X and PDMS-Y was clearly asymmetric and dependent on the position of the scaffolds (Fig. 7A and movie S1). In particular, the arms parallel to the PDMS channels were more deformed than the one perpendicular to them, demonstrating the influence of alignment due to the presence of the PDMS. More interesting was the effect of the rotated director field by having PDMS scaffolds at 45°. Instead of adhering to the originally programmed orthogonal cross design, the rotated channel induced a diagonal skew in the gripper's configuration. In this configuration, the gripper's two arms were initially positioned closely to each other, with each pointing toward one side of the PDMS surface. During the heating process, the gripper displayed a scissor-like movement with its arms extending toward the open end of the channel. The scissor motion reversed as the temperature cooled down, ultimately returning the gripper to its original state. The extent of this actuation movement, defined by the change in the angle (θ) between the two gripper arms, could reach up to 24°, while the arms of the gripper printed in a pristine configuration remained orthogonal during the activation cycles. As before, the observations are compared with the predictions of nonlinear morphoelasticity, which again reveals the essential features of the experimental actuation. The cross experiences a shearing along its four arms, with the largest displacements at its ends. This results in the same scissor-like motion as that which was experimentally observed. Simulations thus confirm that the fabricated microactuators deform as prescribed by the nematic orientation, demonstrating that the method is effective in programming mechanical actuation. This method can be extended to other geometries and alignment patterns by adhering to the boundary conditions of the PDMS scaffolds, as demonstrated with LC solvent. As shown in fig. S5, a flat disc printed within cylindrical scaffolds exhibited up-folding deformation upon heating when the cavity diameter was 50 μm. When the diameter exceeded 70 μm, the disc expanded horizontally, similar to the pristine ones. These observations of different actuator behaviors are consistent with the director field shown in Fig. 3 (see section S5 and movie S2).

DISCUSSION

Here, we introduced a simple workflow for tailoring LC alignment in 3D and then fixing it in a 3D-printed microstructure, so that it finally can be actuated by temperature. The method relied on exploiting the surface characteristics of PDMS, which influences the orientation of the LC molecules throughout the sample. Using the PDMS microstructures as confining scaffolds, the LC directors arranged according to the influence of their specific geometries and as predicted by Landau de Gennes theory, resulting in LC topologies of varied complexity which could not be achieved with the conventional surface alignment method. The achieved alignment patterns were then fixed in 3D-printed microstructures. Their actuation was correctly predicted by an elasticity theory with spatially varying metrics.

Our workflow allows us to generate microactuators in a simple 3D-printing setup that does not require any additional instrumental or manufacturing modification. Specifically, we have demonstrated the capability to fabricate various 4D microstructures, such as pillar arrays and more complex grippers, which exhibit the desired actuation by controlling their alignment in 3D. By combining alignment patterns with specific geometries, we believe that a large and rich design space for potential applications can be created in the near future. Given that PDMS is widely used in biomedical systems, such as microfluidic chips (*44*), incorporating multiple LCE-printed components offers the opportunity, e.g., to fabricate adaptable valves for modulating fluidic channels or cell sorting (*45*) or to incorporate our microscaffolds into multicellular tissue. For such applications, high temperatures are problematic and the transition temperature should be lowered by new formulations. Furthermore, incorporating photoresponsive units within the LCE formulation would enable temporal and spatial control over each individual microactuator (*13*), thus advancing microrobotics. In addition, developing strategies to selectively remove the PDMS microscaffolds would further eliminate geometric limitations and open this workflow for combination with other structures or procedures. Potential approaches for scaffold removal include selective etching (see fig. S7 for proof of principle) or incorporating photocleavable units (*46*) within the PDMS network.

Since both alignment and the effect of actuation can be described by appropriate theories, the door is now open for rational design of 4D-printing solutions, including the possibility to use machine learning approaches to achieve desired design features, in analogy to similar developments in the field of nanophotonics (*47*).

MATERIALS AND METHODS

Chemicals and materials

Liquid crystalline compounds, including 4-methoxybenzoic acid, C6BP, C6BAPE, RM257, 1,4 bis[4-(6-acryloyloxyhexyloxy)benzoyloxy]-2-methylbenzene, and the LC mixture E7 were purchased from

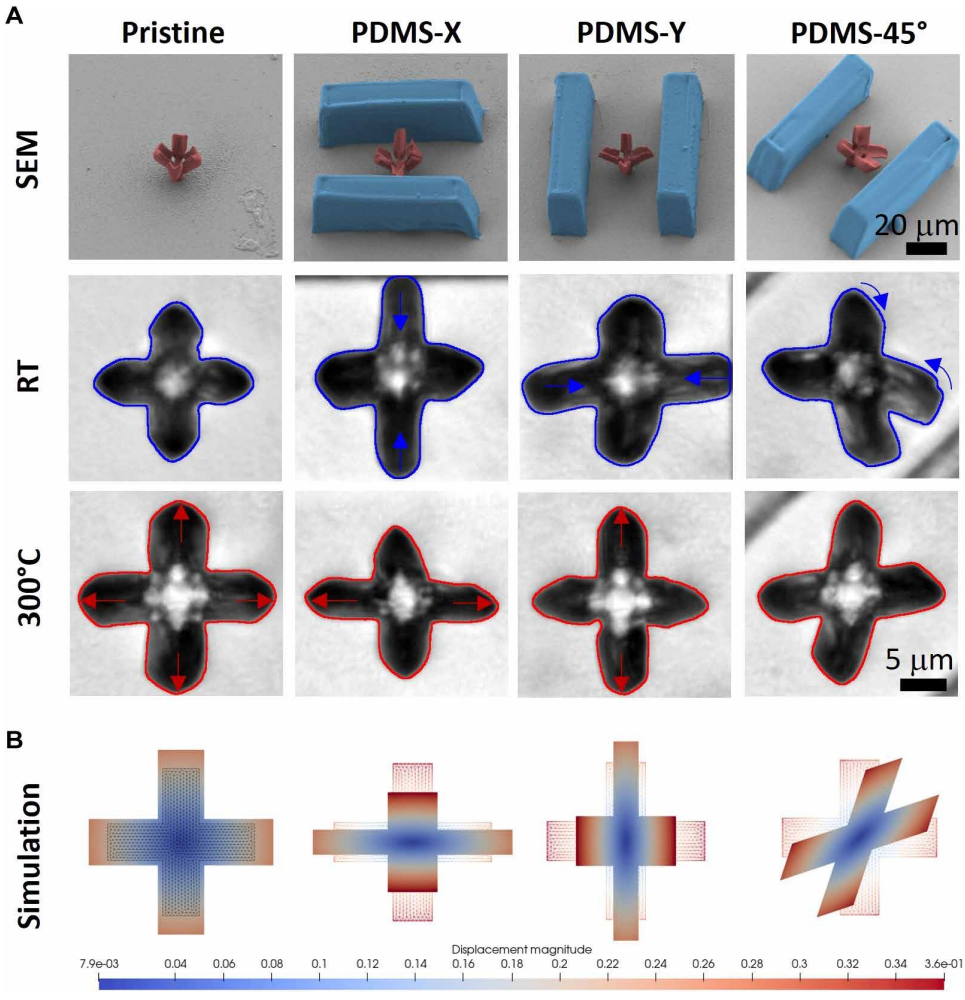

Fig. 7. 4D microgripper with different alignments. (**A**) LCE microgripper printed without (pristine) or within PDMS microchannels with varied orientation, exhibiting distinct thermal activation once the structures were heated from room temperature (RT) to 300°C. The blue and red arrows indicate the deforming direction of the gripper, corresponding to the geometry differences between the (**B**) simulated initial state (translucent) and the simulated activated state (saturated). The simulated mechanical actuation and resulting displacement magnitude was based on a simplified geometry and a hyperelastic material which has a uniform director field with perpendicular orientation to the PDMS scaffold. Units are rescaled so that the length of the sides of the cross are 1. See movie S1.

SYNTHON Chemicals GmbH & Co. KG. The photoinitiator [phenylbis(2,4,6-trimethylbenzoyl)phosphine oxide (BAPO)] and a radical inhibitor [3,5-di-tert-4-butylhydroxytoluene (BHT)] were supplied by Sigma-Aldrich. High-performance liquid chromatography grade 2-propanol (99.5%) and dichloromethane (99.7%) were purchased from Thermo Fisher Scientific, and IP-PDMS was acquired from Nanoscribe GmbH & Co. KG. All materials were used as received without further purification.

LC ink preparation

LC inks were prepared by dissolving all LC components (see compositions in table S1), BAPO and BHT in dichloromethane (2 ml). The homogeneous solution was stirred continuously at 65°C under a nitrogen flow for an hour until the solvent was completely removed.

Preparation of alignment surfaces

Microscope cover glasses with dimensions of 22 × 22 mm^2 and a thickness of 170 ± 5 μm (Marienfeld) were sequentially sonicated in acetone and 2-propanol for 10 min each and then treated with a plasma cleaner (Harrick Plasma). To achieve a 90° anchoring of the LC director to the substrate, a 100 μl of polyimide (Nissan SUNEVER SE-5661) was spin-coated onto the glass surfaces at a spinning speed of 300 rpm for 5 s, followed by an acceleration to 4000 rpm for 20 s. The coated substrates were prebaked at 80°C for 2 min and then postbaked at 220°C for 30 min to complete the polymerization.

Alignment cell

The assembly of the alignment cells was adapted from the previously reported procedure (*13*). Before the assembly, each corner of the polyimide-coated substrate was deposited with a ultraviolet (UV)–curable glue (Norland UV Sealant 91), which was previously mixed with soda lime glass microspheres (diameter, 100 μm; Cospheric LLC) to define the cell thickness. Two substrate pieces, with their alignment surfaces facing inward, were then joined and exposed to UV light for 1 min inside an Asiga Flash UV chamber to ensure bonding. The alignment cell was heated to 80°C, at which

point the LC mixture was filled in the cell via capillary force. The cell was gradually cooled to room temperature at a controlled rate of 1°C/min. For aligning polymerizable LC ink, the cell was kept in the dark during the alignment process.

Two-photon laser microprinting

All 3D microstructures were fabricated within a direct laser writing setup (λ = 780 nm, Photonic Professional GT2, Nanoscribe GmbH & Co. KG). PDMS microscaffolds were printed in a dip-in laser lithography (DiLL) configuration. A droplet of IP-PDMS was placed both at the center of the substrate, with the functionalized side facing downward, and on the lens of a 25× objective [numerical aperture (NA) = 0.8 and working distance (WD) = 380 μm; Zeiss]. All PDMS microscaffolds were printed with an optimized profile that a contour shell composed of 12 layers (contour distance, 0.2 μm) was first printed with a laser power of 30 mW and a scanning speed of 20 mm/s, and then followed by the filling of the interior (with a laser power of 40 mW, a scanning speed of 100 mm/s, and slicing and hatching distances of 0.3 μm) for each layer. After the printing step, the excess of IP-PDMS was removed by placing the substrate horizontally, with the printed side facing downward, in two separate 2-propanol baths (each containing 10 ml) consecutively for 10 and 2 min each at room temperature. After drying the printed PDMS structures with a gentle nitrogen flow, the substrate was promptly used to construct a glass cell with another substrate to prevent contamination from dust.

For printing LC microstructure, the alignment cell filled with LC ink was subjected to the printer after the alignment step. LC structures were constructed by using a 63× oil objective (NA = 1.4 and WD = 190 μm; Zeiss) to begin the print at the interface between the LC ink and the bottom glass of the alignment cell. The different 3D microstructures were printed using a laser power range of 20 to 30 mW and a printing speed of 5 to 10 mm/s. It is worth noting that for LCE microstructures with a height greater than 5 μm, a 5% increment in laser power was crucial to compensate for the reduction in laser intensity when printing through a birefringent structure. After the printing, the cell was cut open with a blade, and the unpolymerized ink was removed by immersing the substrate sequentially in two warm 2-propanol (60°C) baths for 10 and 2 min, respectively. The printed microstructures were then gently dried with a nitrogen flow.

Optical microscopy

All printed structures were inspected under optical microscopes with transmitted light. A Leica DM2700 M (Leica Microsystems) or an Axio Imager Z1 (Carl Zeiss AG), which were run with the analytical microscope software LAS X or ZEN, respectively, was used. For polarized images, samples were placed between crossed polarizers in both cases.

Actuation of LCE microstructures

The thermoresponsive behavior of LCE microstructures were investigated within a heating stage (LTS 420, Linkam Scientific Instruments), which was either coupled to the optical microscope DM2700 or a stereomicroscope (Leica Z16 APOA, equipped with a camera EO-5310). The heating cycle was programmed to have the temperature first be sprint up from ambient temperature to 120°C (35°C/min), followed by a steady gradient until 300°C (10°C/min), and then remained constant for 5 min before cooling down to room temperature with the same temperature gradient.

Scanning electron microscopy

Scanning electron microscopy (SEM) images were acquired using a Zeiss Ultra 55 (Carl Zeiss AG) at a primary electron energy of 3 keV. Before imaging, samples were coated with a 12-nm-thick layer of Pt/Pd (80:20) using a sputter coater.

Analysis of LC alignment profile

The alignment profile of LC molecules induced by PDMS within each PDMS microscaffold was quantified using the OD values derived from polarized images. This quantification was carried out using the image analysis software ImageJ. Before the analysis, an OD calibration based on mean gray values was performed with a Kodak No. 3 Calibrated Step Tablet, which consists of 21 steps covering a density range from 0.05 to 3.05 OD. The mean gray value of each step was translated into its corresponding OD value. The accuracy of this calibration was verified by constructing a calibration curve with an R^2 value of 0.99. All POM images were cropped to the region of interest and converted into 8-bit grayscale for analysis.

Supplementary Materials

The PDF file includes:

Supplementary Text
Figs. S1 to S7
Table S1
Legends for movies S1 and S2
References

Other Supplementary Material for this manuscript includes the following:

Movies S1 and S2

REFERENCES AND NOTES

1. M. Carlotti, V. Mattoli, Functional materials for two-photon polymerization in microfabrication. *Small* **15**, e1902687 (2019).
2. S. Palagi, P. Fischer, Bioinspired microrobots. *Nat. Rev. Mater.* **3**, 113–124 (2018).
3. J. Li, M. Pumera, 3D printing of functional microrobots. *Chem. Soc. Rev.* **50**, 2794–2838 (2021).
4. F. Soto, E. Karshalev, F. Zhang, B. E. F. de Avila, A. Nourhani, J. Wang, Smart materials for microrobots. *Chem. Rev.* **122**, 5365–5403 (2022).
5. A.-I. Bunea, D. Martella, S. Nocentini, C. Parmeggiani, R. Taboryski, D. S. Wiersma, Light-powered microrobots: Challenges and opportunities for hard and soft responsive Microswimmers. *Adv. Intell. Syst.* **3**, 2000256 (2021).
6. C. A. Spiegel, M. Hippler, A. Münchinger, M. Bastmeyer, C. Barner-Kowollik, M. Wegener, E. Blasco, 4D printing at the microscale. *Adv. Funct. Mater.* **30**, 1907615 (2020).
7. L.-Y. Hsu, C. A. Spiegel, E. Blasco, *4D Microprinting in Smart Materials in Additive Manufacturing* (Elsevier, San Diego, 2022).
8. M. Chen, M. Gao, L. Bai, H. Zheng, H. J. Qi, K. Zhou, Recent advances in 4D printing of liquid crystal elastomers. *Adv. Mater.* **35**, e2209566 (2023).
9. Y. Xia, G. Cedillo-Servin, R. D. Kamien, S. Yang, Guided folding of nematic liquid crystal elastomer sheets into 3D via patterned 1D microchannels. *Adv. Mater.* **28**, 9637–9643 (2016).
10. H. Aharoni, Y. Xia, X. Zhang, R. D. Kamien, S. Yang, Universal inverse design of surfaces with thin nematic elastomer sheets. *Proc. Natl. Acad. Sci. U.S.A.* **115**, 7206–7211 (2018).
11. T. J. White, D. J. Broer, Programmable and adaptive mechanics with liquid crystal polymer networks and elastomers. *Nat. Mater.* **14**, 1087–1098 (2015).
12. J. M. McCracken, V. P. Tondiglia, A. D. Auguste, N. P. Godman, B. R. Donovan, B. N. Bagnall, H. E. Fowler, C. M. Baxter, V. Matavulj, J. D. Berrigan, T. J. White, Microstructured photopolymerization of liquid crystalline elastomers in oxygen-rich environments. *Adv. Funct. Mater.* **29**, 1903761 (2019).
13. L.-Y. Hsu, P. Mainik, A. Münchinger, S. Lindenthal, T. Spratte, A. Welle, J. Zaumseil, C. Selhuber-Unkel, M. Wegener, E. Blasco, A Facile approach for 4D microprinting of multi-photoresponsive actuators. *Adv. Mater. Technol.* **8**, 2200801 (2023).
14. L. Chen, Y. Dong, C.-Y. Tang, L. Zhong, W.-C. Law, G. C. P. Tsui, Y. Yang, X. Xie, Development of direct-laser-printable light-powered nanocomposites. *ACS Appl. Mater. Interfaces* **11**, 19541–19553 (2019).
15. K.-W. Yeung, Y. Dong, L. Chen, C.-Y. Tang, W.-C. Law, G. C.-P. Tsui, D. S. Engstrøm, Printability of photo-sensitive nanocomposites using two-photon polymerization. *Nanotechnol. Rev.* **9**, 418–426 (2020).

16. Y. Yuan, P. Keller, I. I. Smalyukh, Elastomeric nematic colloids, colloidal crystals and microstructures with complex topology. *Soft Matter* **17**, 3037–3046 (2021).
17. I. DeBellis, S. Nocentini, M. G. DelliSanti, D. Martella, C. Parmeggiani, S. Zanotto, D. S. Wiersma, Two-photon laser writing of soft responsive polymers via temperature-controlled polymerization. *Laser Photon. Rev.* **15**, 2100090 (2021).
18. D. Martella, S. Nocentini, D. Nuzhdin, C. Parmeggiani, D. S. Wiersma, Photonic Microhand with autonomous action. *Adv. Mater.* **29**, 1704047 (2017).
19. Y. Guo, J. Zhang, W. Hu, M. T. A. Khan, M. Sitti, Shape-programmable liquid crystal elastomer structures with arbitrary three-dimensional director fields and geometries. *Nat. Commun.* **12**, 5936 (2021).
20. H. Zeng, D. Martella, P. Wasylczyk, G. Cerretti, J.-C. G. Lavocat, C.-H. Ho, C. Parmeggiani, D. S. Wiersma, High-resolution 3D direct laser writing for liquid-crystalline elastomer microstructures. *Adv. Mater.* **26**, 2319–2322 (2014).
21. H. Zeng, P. Wasylczyk, G. Cerretti, D. Martella, C. Parmeggiani, D. S. Wiersma, Alignment engineering in liquid crystalline elastomers: Free-form microstructures with multiple functionalities. *Appl. Phys. Lett.* **106**, 111902–111905 (2015).
22. Y. Guo, H. Shahsavan, M. Sitti, 3D microstructures of liquid crystal networks with programmed voxelated director fields. *Adv. Mater.* **32**, e2002753 (2020).
23. S. Varghese, G. P. Crawford, C. W. M. Bastiaansen, D. K. G. de Boer, D. J. Broer, Microrubbing technique to produce high pretilt multidomain liquid crystal alignment. *Appl. Phys. Lett.* **85**, 230–232 (2004).
24. Z. He, G. Tan, D. Chanda, S.-T. Wu, Novel liquid crystal photonic devices enabled by two-photon polymerization [Invited]. *Opt. Express* **27**, 11472–11491 (2019).
25. U. Jagodič, M. Vellaichamy, M. Škarabot, I. Muševič, Surface alignment of nematic liquid crystals by direct laser writing of photopolymer alignment layers. *Liq. Cryst.* **50**, 1999–2009 (2023).
26. A. Martinez, M. Ravnik, B. Lucero, R. Visvanathan, S. Zumer, I. I. Smalyukh, Mutually tangled colloidal knots and induced defect loops in nematic fields. *Nat. Mater.* **13**, 258–263 (2014).
27. A. Martinez, L. Hermosillo, M. Tasinkevych, I. I. Smalyukh, Linked topological colloids in a nematic host. *Proc. Natl. Acad. Sci. U.S.A.* **112**, 4546–4551 (2015).
28. Y. Yuan, A. Martinez, B. Senyuk, M. Tasinkevych, I. I. Smalyukh, Chiral liquid crystal colloids. *Nat. Mater.* **17**, 71–79 (2018).
29. A. Münchinger, V. Hahn, D. Beutel, S. Woska, J. Monti, C. Rockstuhl, E. Blasco, M. Wegener, Multi-photon 4d printing of complex liquid crystalline microstructures by *in situ* alignment using electric fields. *Adv. Mater. Technol.* **7**, 2100944 (2022).
30. A. Münchinger, L.-Y. Hsu, F. Fürniß, E. Blasco, M. Wegener, 3D optomechanical metamaterials. *Mater. Today* **59**, 9–17 (2022).
31. W. Zheng, Y.-T. Hu, Alignment of liquid crystal confined in polydimethylsiloxane channels. *Mol. Cryst. Liq. Cryst.* **615**, 1–8 (2015).
32. W. J. Zheng, M. H. Huang, Use of polydimethylsiloxane thin film as vertical liquid crystal alignment layer. *Thin Solid Films* **520**, 2841–2845 (2012).
33. K. A. Rutkowska, P. Sobotka, M. Grom, S. Baczyński, M. Juchniewicz, K. Marchlewicz, A. Dybko, A novel approach for the creation of electrically controlled LC: PDMS microstructures. *Sensors* **22**, 4037 (2022).
34. S. Baczyński, P. Sobotka, K. Marchlewicz, M. Słowikowski, M. Juchniewicz, A. Dybko, K. A. Rutkowska, Orientation of liquid crystalline molecules on PDMS surfaces and within PDMS microfluidic systems. *Appl. Sci.* **11**, 11593 (2021).
35. W. Zheng, M.-C. Lee, Attainment of planarly aligned liquid crystal using vertical alignment polymer walls. *Mol. Cryst. Liq. Cryst.* **553**, 28–35 (2012).
36. S. Baczyński, P. Sobotka, K. Marchlewicz, M. Juchniewicz, A. Dybko, K. A. Rutkowska, Study of PDMS microchannels for liquid crystalline optofluidic devices in waveguiding photonic systems. *Crystals* **12**, 729 (2022).
37. P. F. J. van Altena, A. Accardo, Micro 3D printing elastomeric IP-PDMS using two-photon polymerisation: A comparative analysis of mechanical and feature resolution properties. *Polymers* **15**, 1816 (2023).
38. M. Ravnik, S. Žumer, Landau–de Gennes modelling of nematic liquid crystal colloids. *Liq. Cryst.* **36**, 1201–1214 (2009).
39. R. Ondris-Crawford, E. P. Boyko, B. G. Wagner, J. H. Erdmann, S. Žumer, J. W. Doane, Microscope textures of nematic droplets in polymer dispersed liquid crystals. *J. Appl. Phys.* **69**, 6380–6386 (1991).
40. Y. Yuan, M. Tasinkevych, I. I. Smalyukh, Colloidal interactions and unusual crystallization versus de-mixing of elastic multipoles formed by gold mesoflowers. *Nat. Commun.* **11**, 188 (2020).
41. S. Woska, A. Münchinger, D. Beutel, E. Blasco, J. Hessenauer, O. Karayel, P. Rietz, S. Pfleging, R. Oberle, C. Rockstuhl, M. Wegener, H. Kalt, Tunable photonic devices by 3D laser printing of liquid crystal elastomers. *Opt. Mater. Express* **10**, 2928–2943 (2020).
42. W. Zheng, L. Yang, M. Lee, Vertical alignment of liquid crytals on polydimethylsiloxane Thin Films. *Photonics Lett. Pol.* **3**, 8–10 (2011).
43. A. Goriely, L. A. Mihai, Liquid crystal elastomers wrinkling. *Nonlinearity* **34**, 5599–5629 (2021).
44. P. Pattanayak, S.K., Singh, M. Gulati, S. Vishwas, B. Kapoor, D. K. Chellappan, K. Anand, G. Gupta, N. K. Jha, P. K. Gupta, P. Prasher, K. Dua, H. Dureja, D. Kumar, V. Kumar, Microfluidic chips: Recent advances, critical strategies in design, applications and future perspectives. *Microfluid Nanofluidics* **25**, 99 (2021).
45. C. Barwig, A. Sonn, T. Spratte, A. Mishra, E. Blasco, C. Selhuber-Unkel, S. Pashapour, Two-photon direct laser writing of pNIPAM actuators in microchannels for dynamic microfluidics. *Adv. Intell. Syst.* **6**, 2300829 (2024).
46. R. Batchelor, T. Messer, M. Hippler, M. Wegener, C. Barner-Kowollik, E. Blasco, Two in one: Light as a tool for 3D printing and erasing at the microscale. *Adv. Mater.* **31**, e1904085 (2019).
47. Y. Augenstein, T. Repän, C. Rockstuhl, Neural operator-based surrogate solver for free-form electromagnetic inverse design. *ACS Photonics* **10**, 1547–1557 (2023).
48. X. Wang, Y. Zhou, Y.-K. Kim, M. Tsuei, Y. Yang, J. J. de Pablo, N. L. Abbott, Thermally reconfigurable Janus droplets with nematic liquid crystalline and isotropic perfluorocarbon oil compartments. *Soft Matter* **15**, 2580–2590 (2019).
49. R. R. Maity, A. Majumdar, N. Nataraj, Discontinuous Galerkin finite element methods for the Landau–de Gennes minimization problem of liquid crystals. *IMA J. Numer. Anal.* **41**, 1130–1163 (2021).
50. V. Tkachenko, G. Abbate, A. Marino, F. Vita, M. Giocondo, A. Mazzulla, F. Ciuchi, L. De Stefano, Nematic liquid crystal optical dispersion in the visible-near infrared range. *Mol. Cryst. and Liq. Cryst.* **454**, 263/[665]–271/[673] (2006).

Acknowledgments: We thank R. Schröder, I. Wacker, and R. Curticean for access to and training at the electron microscopy facilities. **Funding:** This work was supported by the Deutsche Forschungsgemeinschaft (DFG; German Research Foundation) via the Excellence Cluster "3D Matter Made to Order" EXC-2082/1-390761711 (E.B. and U.S.S.) and Carl Zeiss Foundation through the "Carl-Zeiss-Foundation-Focus@HEiKA" (EB) Kekulé Fellowship by Fonds der Chemischen Industrie (C.V.-M.). **Author contributions:** Conceptualization: L.-Y.H., U.S.S., and E.B. Methodology: L.-Y.H., S.G.M., U.S.S., and E.B. Investigation: L.-Y.H., S.G.M., C.A.S., C.V.-M., F.Z., U.S.S., and E.B. Visualization: L.-Y.H., S.G.M., and C.V.-M. Supervision: U.S.S. and E.B. Writing–original draft: L.-Y.H., S.G.M., U.S.S., and E.B. Writing–review and editing: L.-Y.H., S.G.M., C.A.S., C.V.-M., F.Z., U.S.S., and E.B. **Competing interests:** The authors declare that they have no competing interests. **Data and materials availability:** All data are available in the main text or the Supplementary Materials. Furthermore, all related code and its documentation may be found in the GitHub repository https://github.com/sgomezmelo/Landau-de-Gennes-dGFEM and https://heidata.uni-heidelberg.de/.

Submitted 7 May 2024
Accepted 1 August 2024
Published 6 September 2024
10.1126/sciadv.adq2597